Robotica (2022), **40**, pp. 294–315
doi:10.1017/S0263574721000539

CAMBRIDGE UNIVERSITY PRESS

RESEARCH ARTICLE

Bimodal mobility actuated by inertial forces with surface elastic bodies in microgravity

Kenji Nagaoka[1]*, Toshiyasu Kaneko[2], and Kazuya Yoshida[2]

[1]Department of Mechanical and Control Engineering, Graduate School of Engineering, Kyushu Institute of Technology, Fukuoka, Japan
[2]Department of Aerospace Engineering, Graduate School of Engineering, Tohoku University, Sendai, Japan
*Corresponding author. Email: nagaoka@ieee.org

Received: 10 January 2020; **Revised:** 11 April 2021; **Accepted:** 12 April 2021; **First published online:** 11 May 2021

Keywords: bimodal mobility, inertial forces, elastic bodies, eccentric motor, microgravity

Abstract

This paper presents bimodal mobility actuated by inertial forces with elastic bodies for an exploration robot in a microgravity environment. The proposed bimodal locomotion mechanism can selectively achieve vibration propulsion or rotational hopping mode based on centrifugal force and reaction torque exerted by the control of a single eccentric motor, where the rotational hopping is the primary locomotion mode for practical applications. The bimodal mobility performance under microgravity is experimentally examined using an air-floating testbed. Furthermore, we also present theoretical modeling of the bimodal mobility system, and the model is verified by comparison with the experiments.

1. Introduction

Exploration robots enable to achieve continuous scientific observation with higher resolution on multiple areas of extraterrestrial surfaces. Surface mobility is an essential technology for the robots. Achieving adaptive surface mobility on minor bodies with extremely low gravity fields, such as asteroids or comets, is technically challenging. On such bodies, wheels or tracks are highly inefficient and ineffective for robotic mobility because of microgravity. Typical examples of mobile robots or landers for minor body exploration are PROP-F [1] in the Phobos 2 mission and MINERVA [2] in the Hayabusa mission. Both used hopping mobility and failed to land onto the surface. Following the Hayabusa mission, the Hayabusa 2 spacecraft operated by JAXA [3] carries three MINERVA-II rovers [4, 5] and MASCOT [6] equipped with surface mobility, mainly hopping mobility. The MINERVA-II-1 rovers and MASCOT successfully demonstrated the reaction torque-based rotational hopping mobility on the asteroid Ryugu [7, 8]. With these practical hopping robots, various hopping mechanisms have been proposed for robotic exploration in microgravity [9, 10, 11, 12]. In principle, motion convergence of these hopping mechanisms is achieved by multiple rebounding on the surface . Hence, it is difficult for the robots to accurately access a destination without a soft-landing mechanism. The conventional hopping robots have been designed to give more priority to locomotion reliability than to destination accessibility on minor bodies.

Meanwhile, we have applied a vibration propulsion mechanism actuated by a small eccentric motor with surface elastic bodies to the robotic mobility in microgravity. [13, 14, 15] Vibration propulsion is generated by inducing motor vibrations on inclined elastic bodies, such as a linear actuator [16, 17], a micro-robot [18, 19, 20, 21], a conveyor [22], and an active scope camera [23]. Hence, this mobility mechanism improves destination accessibility based on crawling motion. We have showed it is an applicable locomotion technique on frictional low slope with microscale roughness from sub-millimeters to

several millimeters [15]. With the latest observation of a highly rugged terrain of Ryugu [7], this mechanism is expected to be used as a secondary locomotion mode on relatively smoother areas. Furthermore, theoretically, conventional dynamics models cannot adequately simulate gravity effects and microscale behaviors on an elastic body.

A robotic mobility system must also possess adaptability to rough terrains. Generally, adaptive mobility, like with animals, is exerted by functionally controlling a multi-degree-of-freedom system. To achieve such adaptability in mobile robots, one usually needs to have several actuators (e.g., a multi-limbed free-climbing robot [24, 25, 26]). With strict limitations on available resources for space applications, however, simultaneous pursuit of adaptive mobility and reduction of the number of actuators is still technically challenging. Accordingly, in this paper, we propose bimodal mobility actuated by a single eccentric motor with surface elastic bodies . The proposed mobility can selectively perform vibration propulsion and rotational hopping motion by controlling inertial forces, centrifugal forces, and reaction torques. These inertial forces are simultaneously generated on a different physical dimension of the motor rotation: rotational acceleration and velocity squared. The key idea of the bimodal mobility is that the different locomotion mode can be achieved by dominantly exerting either the centrifugal force or the reaction torque. In the proposed bimodal mobility system, the rotational hopping is the primary locomotion mode and the vibration propulsion is the secondary one. This paper elaborates the bimodal mobility mechanism based on experimental and theoretical analyses and demonstrates its feasibility. Moreover, we address dynamic modeling of the bimodal mobility such that both the gravity effects on the locomotion and the microscale behaviors of the elastic body can be simulated.

This paper is organized as follows. Section 2 presents the locomotion principle of bimodal mobility, vibration propulsion, and rotational hopping, actuated by the inertial forces with surface elastic bodies in microgravity. We describe a basic framework of the experimental environment that can simulate planar robot motion under microgravity. Section 3 elaborates the mobility performance of the vibration propulsion mode in microgravity based on experimental and theoretical analyses. The comparative discussion exhibits the mobility performance more systematically. Section 4 also presents experimental and theoretical analyses of the rotational hopping mode. Its mobility performance is analyzed via both the experiment and simulation as in Section 3. In Section 5, we discuss a synthetic correlation between inertial forces and the resulting bimodal mobility. The correlation is experimentally and numerically examined. Thus, the bimodal mobility mechanism in microgravity is clarified more systematically. Section 6 summarizes the results and contributions of this paper.

2. Bimodal mobility

2.1. Fundamental principle

In this paper, we propose a novel bimodal surface mobility mechanism using inertial forces and surface elastic bodies under microgravity, whereas each mobility has been demonstrated independently. The proposed mobility mechanism takes advantage of both centrifugal force and reaction torque, which are exerted by a single eccentric motor, and thereby can achieve different locomotion modes. Thus, it is expected to produce more adaptive mobility to unstructured terrains without increasing the number of actuators. This section delivers the fundamental locomotion principle of the proposed bimodal mobility concept.

A conceptual principle of bimodal mobility is illustrated in Fig. 1. The robotic system is comprised of a rigid main body, surface elastic bodies, and an eccentric motor installed in the main body. For the basic locomotion mode, the robot can selectively perform vibration propulsion or rotational hopping by controlling the motor rotation. Figure 1(b) shows a typical time-series relationship between the input motor rotation and the output inertial forces. Here, ω_{Md}, F_{Md}, and T_{Md} are defined as the absolute value of the effective motor angular velocities, the effective centrifugal forces, and the effective reaction torques for locomotion, respectively. In this paper, we focus on this typical input condition of the

https://doi.org/10.1017/S0263574721000539 Published online by Cambridge University Press

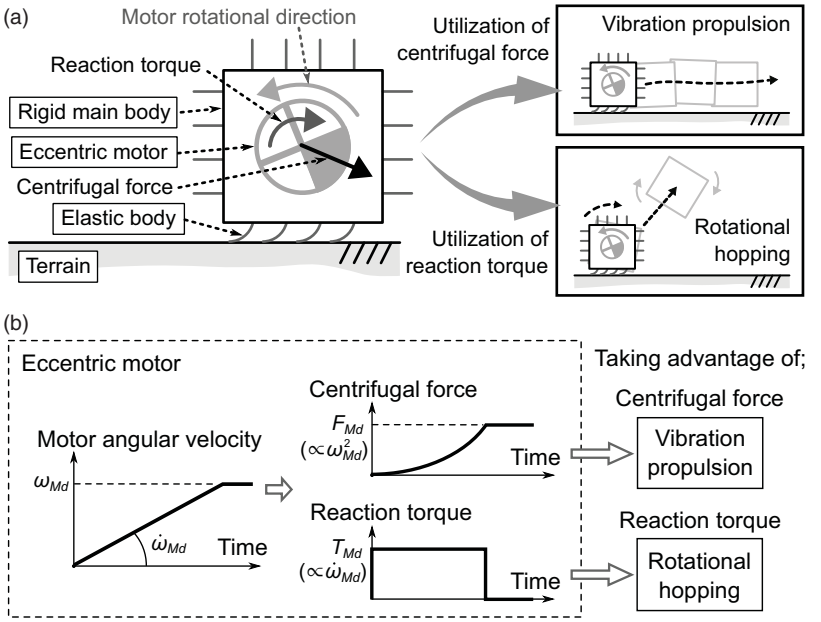

Figure 1. *Conceptual principle of bimodal mobility actuated by inertial forces and elastic bodies in microgravity: (a) fundamental idea of bimodal mobility; (b) typical time histories of rotational conditions and inertial forces of an eccentric motor.*

eccentric motor. Regarding basic application scenarios of the proposed mechanism, the robot utilizes vibration propulsion on a relatively smooth surface. In this situation, a small reaction torque must be simultaneously maintained so that the robot maintains stable locomotion without unexpected rotation. In contrast, on rough or rocky terrain, the robot utilizes the rotational hopping mode by taking advantage of the reaction torque. Thus, the robot enables more adaptive mobility to unstructured terrain under microgravity, such as on asteroids. Such bimodal mobility by a single actuation is expected to contribute to the enhancement of robotic exploration for space applications, whose available resources are limited.

2.2. Demonstration equipment

2.2.1. Experimental environment

The experimentation for demonstration of the bimodal locomotion under microgravity is outlined below. Figure 2(a) shows the experimental environment that can simulate motion under planar microgravity. The inertial coordinate system, $\Sigma_I\{X,\ Y,\ Z\}$, is defined and fixed on the stone plate having 1×1 m in the X-Y plane. An air-floating testbed is used to simulate planar robot motion in microgravity. The testbed can freely move in the X-Y plane on the plate, and microgravity works in the negative direction of the Y-axis. The level of the planar microgravity is adjusted by changing the inclination angle of the stone plate. As a simulated ground surface, a rigid and flat plate is fixed on the side of the stone plate, where plastic tape was attached on its surface to simulate a uniform frictional characteristic.

In the experiments, several camera systems are used. A webcam records the overview motion of the testbed, which takes a downward view normal to the X-Y plane. An external motion capture camera system is also used for tracking the testbed motion. The sampling frequency of the tracking system is 100 Hz, and its position detecting accuracy is less than 0.1 mm in the following experiments. Additionally, a

https://doi.org/10.1017/S0263574721000539 Published online by Cambridge University Press

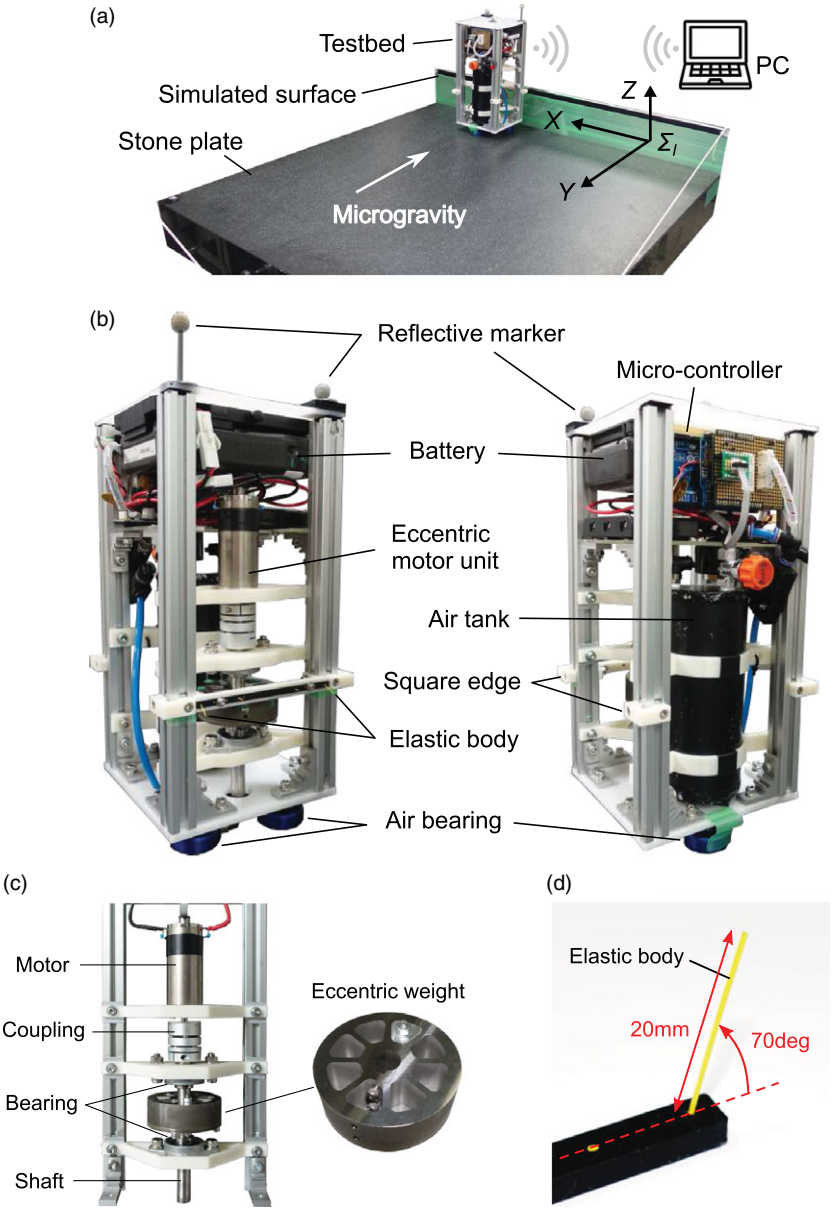

Figure 2. *Experimental environment for simulating planar robot motion in microgravity on ground: (a) overview, (b) air-floating testbed (from two viewpoints), (c) eccentric motor unit, and (d) elastic body.*

high resolution digital camera is used to observe the microscale behavior of the elastic body during the experiments. The frame rate and resolution are set to 30 fps and 3840×2160 pixel, respectively.

2.2.2. Air-floating testbed

Figure 2(b) shows the air-floating testbed that simulates planar motion under microgravity. The testbed has a weight of 4.32 kg, a moment of inertia of 1.54×10^{-2} kgm^2, and a size of 15 × 15 cm in the *X*-*Y* plane. The motor embedded in the testbed is a brushed DC motor (DCX32L, produced by maxon

https://doi.org/10.1017/S0263574721000539 Published online by Cambridge University Press

motor ag.) whose shaft is connected to an eccentric weight via clamp-coupling, as shown in Fig. 2(c). The eccentric weight has a diameter of 65 mm and a height of 23 mm. Its weight, moment of inertia, and eccentric distance from the rotational axle can be physically changed by adding small weights into the spaces. Moreover, the testbed has a micro-controller with a battery. Therefore, we can remotely control it via wireless communications. Throughout the experiments, we obtain time-series data of the motor rotational angle.

Regarding surface elastic bodies, two polypropylene wire rods, whose diameter is 0.5 mm, are used. They are attached onto the side of the testbed as shown in Fig. 2(a). According to our previous work [13, 14, 15], as a benchmark of feasible design parameters of an elastic body, their inclination angle and natural length are, respectively, determined to be 70° and 20 mm, as shown in Fig. 2(d).

2.2.3. Microgravity environment

In the following experiments, the microgravity in the Y-axis direction is simulated such that the relative error from the desired value becomes less than a ±5%. With respect to the microgravity in the X-axis direction, it is set to approximately 10^{-5} G to not militate against the testbed motion.

3. Vibration propulsion

This section first presents motion analyses of the vibration propulsion mode based on the microgravity experiments. Then, it models the vibration propulsion. Furthermore, comparative analyses of the experiments and numerical simulations are elaborated. To discuss the motion with a steady-state velocity, the resulting time-history data of vibration propulsion are shown as $t = 0$ (s) at the beginning of the steady state.

3.1. Experimental analysis

3.1.1. Conditions

The vibration propulsion is experimentally analyzed. The experiments focus on effects of microgravity on locomotion performance, including motion behaviors of the elastic body, which are not previously examined. The effective motor rotational frequency was set to 2 Hz (i.e., $\omega_{Md} = 4\pi$ (rad/s)) for ease of observation of the microscale behaviors of the elastic body. The microscale motion of the elastic body was analyzed using a kernelized correlation filter of OpenCV. The motor rotates in a counterclockwise direction around the Z-axis. The experimental conditions were set as follows.

- g: 7.5×10^{-4}, 1.0×10^{-3}, 1.25×10^{-3}, 1.5×10^{-3} G
- F_{Md} ($= m_e r_e \omega_{Md}^2$): 0.092, 0.164, 0.219 N
- T_{Md}: 0.002 Nm

Here, g is the gravity acceleration, m_e is the mass of the eccentric motor, and r_e is the distance between the center of mass (CoM) of the eccentric weight and the motor axle, respectively. In this work, the motor rotational velocity was controlled to follow the ideal time histories shown in Fig. 1(b). In the experiments, three different values of effective centrifugal force were applied by changing additional weight of the eccentric weight. Furthermore, the experiments in each condition were conducted four times. Hence, an average value of the resulting data is evaluated with an error bar of standard deviation.

3.1.2. Results and discussion

Figure 3 depicts the averaged locomotion velocity of the testbed in the X-axis direction against the microgravity condition; each experimental plot involves an error bar. Here, the locomotion velocity was evaluated by a steady-state value of when the testbed moves at a steady velocity. This result shows that a larger effective centrifugal force provides larger locomotion velocity in all gravitational cases. Additionally, the locomotion velocity decreases with an increase in gravity acceleration within the

https://doi.org/10.1017/S0263574721000539 Published online by Cambridge University Press

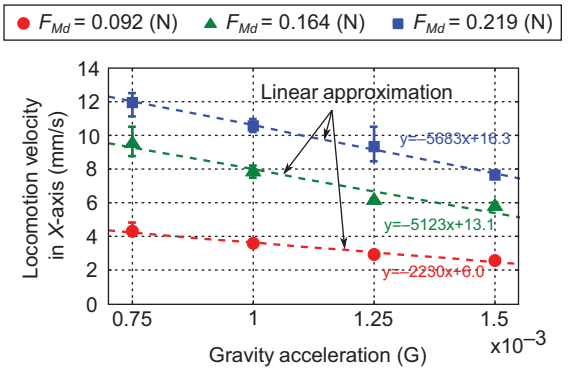

Figure 3. *Experimental locomotion velocity of vibration propulsion under several microgravity conditions.*

experimented microgravity range. This shows a linear relationship and a larger centrifugal force case is more sensitive to change of gravity.

Microscale observation. The microscale motion behavior of the elastic body was analyzed by the captured camera images. To compare the effect of gravity, the analysis focuses on the conditions of $F_{Md} = 0.219$ (N) and $g = 7.5 \times 10^{-4}$, 1.5×10^{-3} (G) in Fig. 3. As a typical example, Fig. 4(a) shows the motion snapshot of the front elastic body under $g = 7.5 \times 10^{-4}$ (G). Furthermore, Fig. 4(b) shows 5-s motion profiles of the front elastic body under each gravity condition.

For a global behavior analysis, the elastic body shows a regular stick-slip motion in the relatively larger microgravity. Meanwhile, it shows a cyclic motion in the relatively smaller microgravity. In both the gravities, the motion was synchronized with a motor rotation frequency of 2 Hz. These profiles confirm that the tip of the elastic body always contacts the ground surface in the larger gravity, whereas the elastic body hops to 2 mm in height. Accordingly, we define the motion (or sub-mode) shown in Fig. 4(a) and (b) as micro-hopping and crawling, respectively. The micro-hopping motion is also defined as the state in which one or both elastic bodies float above the ground and comes from the resonant characteristic of elasticity of the elastic body [15]. With analysis results of other gravity conditions, the crawling motion is a major mode in the larger gravity, and the proportion of micro-hopping on the global motion increased with a decrease in gravity. In the vibration propulsion mode actuated by a constant centrifugal force, the elastic body motion continuously transits from crawling to micro-hopping with a reduction of microgravity.

For local behavior analysis, the bending deflection and buckling (i.e., flexural deformation) of an elastic body is smaller in the micro-hopping motion, because of the smaller gravity, as shown in Fig. 4. By contrast, its equilibrium deformation becomes larger in the crawling motion because of the larger gravity. Hence, the elastic force exerted by the elastic body is relatively larger in the crawling motion, because of a larger normal force reacting from the ground to the testbed. This increase in the normal force produces an increase in the friction between the elastic body and the ground surface. Thus, this frictional difference results in velocity characteristics.

Vibration propulsion mechanism. The locomotion principle of vibration propulsion mechanism is organized below. From quantitative motion behaviors, the testbed motion is divided into the following four phases, as shown in Fig. 5.

- Micro-hopping:

(1) The testbed moves forward and squats downward via the centrifugal force of the eccentric motor, where the elastic body sticks and bends, and thereby propels the testbed forward.

https://doi.org/10.1017/S0263574721000539 Published online by Cambridge University Press

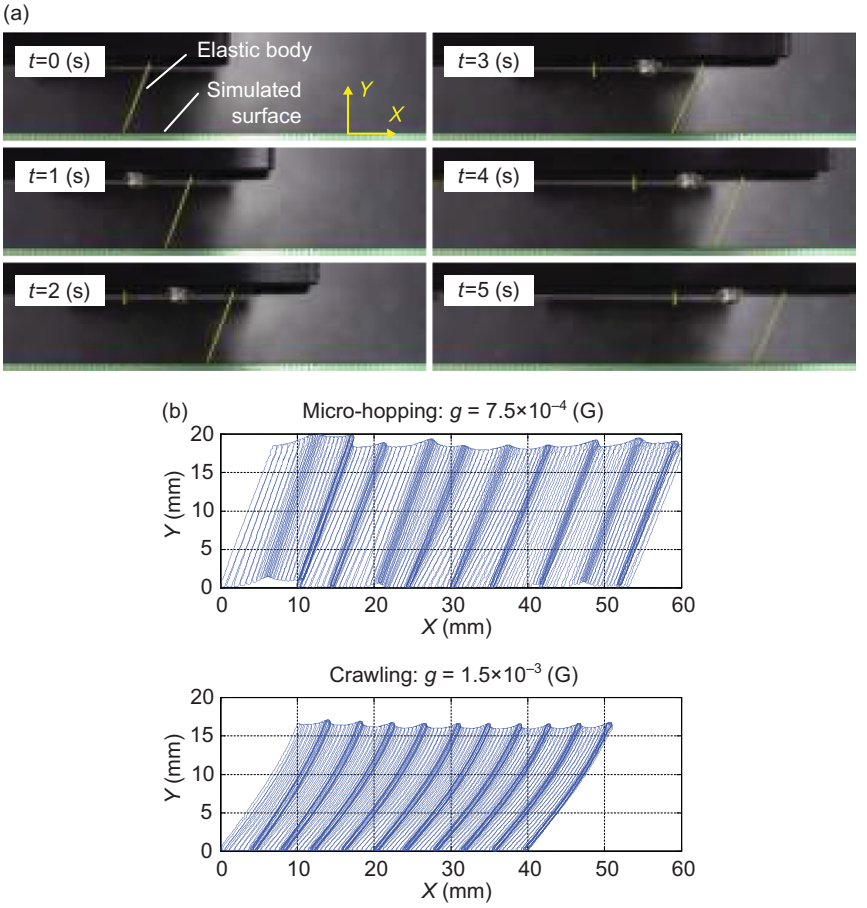

Figure 4. *Experimental results of the front elastic body motion during vibration propulsion: (a) motion snapshots under $g = 7.5 \times 10^{-4}$ (G); (b) 5-s motion profiles based on image processing.*

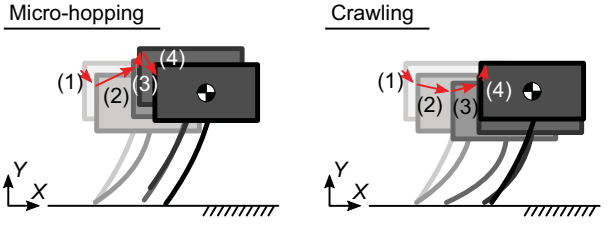

Figure 5. *Schematic sequence of vibration propulsion mechanism: micro-hopping motion and crawling motion.*

(2) The testbed performs micro-hopping upward and forward by releasing elastic energy stored in the elastic body.
(3) The micro-hopping direction increases upward with decreased velocity via the centrifugal force.
(4) The testbed lands softly on the ground.

• Crawling:

(1) The testbed moves forward and squats downward via the centrifugal force of the eccentric motor, where the elastic body sticks and bends, and thereby propels the testbed forward.

https://doi.org/10.1017/S0263574721000539 Published online by Cambridge University Press

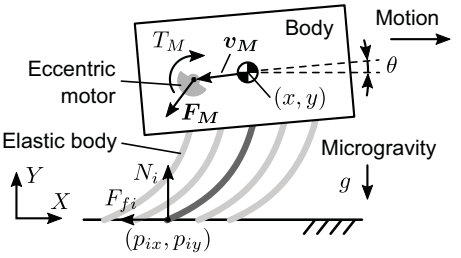

Figure 6. *Dynamics model for robot in vibration propulsion mode.*

(2) The elastic body slips forward, where the testbed continues moving forward and squats downward. Simultaneously, the elastic body accelerates forward via the centrifugal force while increasing the normal force to the ground. Thus, the testbed moves while increasing kinetic frictional resistance between the elastic body on the ground.
(3) The testbed moves upward and forward with decreased forward velocity as the elastic body recovers from its bending deflection and buckling.
(4) The testbed moves upward and the elastic body recovers from the deflection and buckling by the centrifugal force.

The testbed motion clearly synchronizes with the change of centrifugal force. Moreover, the testbed results in the forward movement caused by friction anisotropy between the inclined elastic body and the ground surface.

3.2. Modeling

3.2.1. Equation of motion

In this paper, we focus on planar model for robot motion. Figure 6 illustrates the planar robot model for the vibration propulsion. For planar motion modeling, the CoM position of the robot is defined as (x, y) in the inertial coordinate, $\Sigma_I\{X, Y\}$, where the origin of the Y-axis is set to the terrain surface. Let the robot attitude angle be θ, where the counterclockwise direction is positive. Whereas two elastic bodies are attached on the testbed, the number of the elastic bodies is modeled as N for generality, where an i-th elastic body is represented by a subscript, i.

The equations of motion of the robot are given as follows:

$$M\ddot{x} = \sum_{i=1}^{N} F_{fi} + F_{Mx}, \tag{1}$$

$$M\ddot{y} = \sum_{i=1}^{N} N_i + F_{My} - Mg, \tag{2}$$

$$I\ddot{\theta} = \sum_{i=1}^{N} \left\{ N_i(p_{ix} - x) - F_{fi}(p_{iy} - y) \right\} + \boldsymbol{v_M} \times \boldsymbol{F_M} - T_M, \tag{3}$$

where M is the robot mass, I is the moment of inertia of the robot, F_{fi} is the friction force acting on the tip of the i-th elastic body, N_i is the normal force acting on the tip of the i-th elastic body, $\boldsymbol{p_i}(p_{ix}, p_{iy})$ is the tip position of the i-th elastic body, $\boldsymbol{v_M}$ is the position vector from the robot CoM to the rotational axis of the motor, $\boldsymbol{F_M}(F_{Mx}, F_{My})$ is the centrifugal force exerted by the motor in Σ_I, T_M is the driving torque exerted by the motor, and subscripts x and y denote the X- and Y-axes components of each variable, respectively.

https://doi.org/10.1017/S0263574721000539 Published online by Cambridge University Press

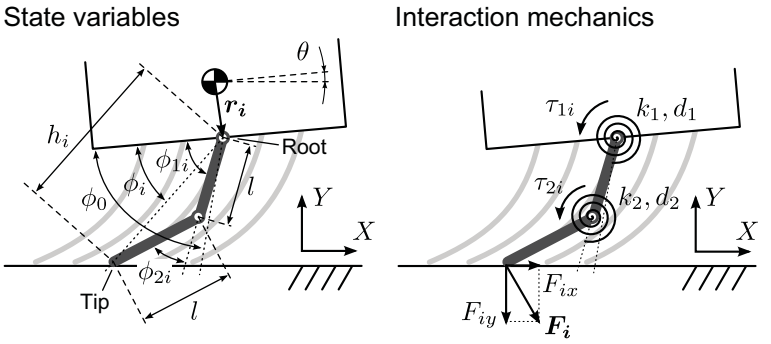

Figure 7. *Dynamics model of surface elastic body.*

3.2.2. Inertial force of eccentric motor

As the inertial forces, the centrifugal force and reaction torque exerted by an eccentric motor are modeled. The centrifugal force, $\boldsymbol{F_M}(F_{Mx}, F_{My})$, is given as follows:

$$F_{Mx} = F_M \cos(\theta_M + \theta),\ F_{My} = F_M \sin(\theta_M + \theta), \tag{4}$$

where $F_M = m_e r_e \omega_M^2$ and θ_M is the motor angle in relative coordinates fixed in the robot base and $\dot{\theta}_M = \omega_M$.

In the robot model, a DC motor is assumed, and its driving torque, T_M, is given as follows:

$$T_M = (J_M + \nu_M)\ddot{\theta}_M + T_r, \tag{5}$$

where J_M is the entire moment of inertia of the motor rotor with the eccentric weight, ν_M is the motor's damping coefficient, and T_r is the external torque resistance. Here, ν_M can be assumed to be ideally 0 when a gear-head is not embedded in the motor. T_r is also approximated to be zero, owing to $g << 1$. Accordingly, the motor torque can be given as follows:

$$T_M \approx J_M \ddot{\theta}_M, \tag{6}$$

where the reaction torque, $-T_M$, acts on the robot.

3.2.3. Contact force

To formulate the reaction forces, N_i and F_{fi}, the deformation change of elastic body must first be introduced. In this paper, we represent the elastic body as a two-link system with rotational viscoelastic joints, as illustrated in Fig. 7.

The joint angles, ϕ_{1i} and ϕ_{2i} of the elastic body, can be expressed as follows:

$$\phi_{1i} = \phi_i + \cos^{-1}\left(\frac{h_i}{h_0}\right),\quad \phi_{2i} = 2\cos^{-1}\left(\frac{h_i}{h_0}\right), \tag{7}$$

where h_0 is the natural length of the elastic body, and ϕ_i and h_i are, respectively, defined as the equivalent joint angle and length of the elastic body, as shown in Fig. 6. h_i is given as follows:

$$h_i = \sqrt{\left(x + r_{ix}\cos\theta - r_{iy}\sin\theta - p_{ix}\right)^2 + \left(y + r_{iy}\sin\theta + r_{iy}\cos\theta\right)^2}, \tag{8}$$

where $\boldsymbol{r_i}(r_{ix}, r_{iy})$ is the vector from the robot CoM to the base position of elastic body. ϕ_i is also defined as the angle between the robot base and the line connecting the tip and root of the elastic body, and can be given as follows:

$$\phi_i = \tan^{-1}\left(\frac{y + r_{ix}\sin\theta + r_{iy}\cos\theta}{x + r_{ix}\cos\theta - r_{iy}\sin\theta - p_{ix}}\right) - \theta. \tag{9}$$

https://doi.org/10.1017/S0263574721000539 Published online by Cambridge University Press

Hence, the displacement of the first joint, $\Delta\phi_{1i}$, and the second joint, $\Delta\phi_{2i}$, is written by

$$\Delta\phi_{1i} = \phi_0 - \phi_{1i}, \quad \Delta\phi_{2i} = \phi_{2i}. \tag{10}$$

where ϕ_0 is the angle of ϕ_{1i} in the undeformed state.

Given that k_j and d_j are, respectively, the elastic stiffness and viscous damping of joint j ($j = 1, 2$) of the elastic body shown in Fig. 6, the joint's viscoelastic torque, $\boldsymbol{\tau_i}(\tau_{1i}, \tau_{2i})$, can be expressed as follows:

$$\tau_{1i} = k_1(\phi_0 - \phi_{1i}) - d_1\dot{\phi}_{1i}, \ \tau_{2i} = k_2\phi_{2i} + d_2\dot{\phi}_{2i}. \tag{11}$$

By the moment equilibrium about the joints, an elastic force, $\boldsymbol{F_i}(F_{ix}, F_{iy})$, acting on the tip of elastic body, can be represented as follows:

$$\begin{cases} F_{ix} = \dfrac{\tau_{1i}\cos\psi_{2i} - \tau_{2i}\,(\cos\psi_{1i} + \cos\psi_{2i})}{l\sin\phi_{2i}}, & \text{(12a)} \\ F_{iy} = \dfrac{-\tau_{1i}\sin\psi_{2i} + \tau_{2i}\,(\sin\psi_{1i} + \sin\psi_{2i})}{l\sin\phi_{2i}}, & \text{(12b)} \end{cases}$$

where $\psi_{1i} = \phi_{1i} + \theta$, $\psi_{2i} = \psi_{1i} - \phi_{2i}$, the link length, l, is constant ($l = h_0/2$), and $\phi_{2i} \neq 0$ is assumed to be satisfied during contact. The friction force, F_{fi}, acting on the tip of the i-th elastic body, can also be modeled as follows:

$$F_{fi} = \begin{cases} 0 & \text{for } p_{iy} > 0 \text{ (w/o contact)}, & \text{(13a)} \\ F_{ix} & \text{for } p_{iy} \le 0 \wedge \dot{p}_{ix} = 0 \text{ (sticking)}, & \text{(13b)} \\ -\mu_d' N_i & \text{for } p_{iy} \le 0 \wedge \dot{p}_{ix} > 0 \text{ (slip forward)}, & \text{(13c)} \\ \mu_d' N_i & \text{for otherwise (slip backward)}, & \text{(13d)} \end{cases}$$

where the normal force is given as $N_i = F_{iy}$ and μ_d' is the apparent kinetic frictional coefficient. Generally, the elastic body model has friction anisotropy [16, 27, 28]; μ_d' can be represented as follows:[16].

$$\mu_d' = \begin{cases} \dfrac{\mu_d}{1 - \mu_d\tan\psi_{2i}} & \text{for } \dot{p}_{ix} \le 0, & \text{(14a)} \\ \dfrac{\mu_d}{1 + \mu_d\tan\psi_{2i}} & \text{for otherwise}, & \text{(14b)} \end{cases}$$

where μ_d is the kinetic friction coefficient.

3.2.4. Elastic body shape

To calculate the contact force, the tip position of the elastic body is derived based on elastic potential energy.

Contact detection. For the contact detection, the vertical tip position, p_{iy}, which is given by the following, is discussed.

$$p_{iy} = y + r_{ix}\sin\theta + r_{iy}\cos\theta - h_0\sin(\phi_0 + \theta)\,. \tag{15}$$

When $p_{iy} \le 0$, the contact force is calculated based on the subsequent steps.

Stick-slip detection. The contact state is divided into four conditions, depending on the state of the elastic body in one calculation step prior.

(b-1) Case (i): $p_{iy} > 0$ in the previous step: As the contact position between the tip of elastic body and the ground surface, p_{ix} in the current step is calculated based on only the previous step. With p_{ix}, the reaction force, $\boldsymbol{F_i}$, acting on the elastic body, is calculated. Then, by comparing F_{ix} and the maximum

https://doi.org/10.1017/S0263574721000539 Published online by Cambridge University Press

static friction, the stick-slip state is detected: stick for $|F_{ix}| \leq \mu_s' N_i$, slip forward for $F_{ix} > \mu_s' N_i$, and slip backward for otherwise. Here, μ_s' is the apparent static frictional coefficient and $\mu_s' N_i \geq 0$. As with the apparent kinetic friction, μ_s' can be represented as follows:

$$\mu_s' = \begin{cases} \dfrac{\mu_s}{1 - \mu_s \tan \psi_{2i}} & \text{for } \dot{p}_{ix} \leq 0, \quad (16a) \\ \dfrac{\mu_s}{1 + \mu_s \tan \psi_{2i}} & \text{for otherwise,} \quad (16b) \end{cases}$$

where μ_s is the static friction coefficient. When stick is detected, the tip position is constrained at the contact point. In the other cases, the simulation goes to the next calculation step.

(b-2) Case (ii): $p_{iy} \leq 0 \wedge \dot{p}_{ix} = 0$ in the previous step: The stick-slip detection is evaluated using the tip position in the previous step, based on the same procedure with Case (i), because the robot body moves and the elastic body is deformed.

(b-3) Case (iii): $p_{iy} \leq 0 \wedge \dot{p}_{ix} > 0$ in the previous step: The elastic body is assumed to slip forward in the $+X$ direction, and the simulation goes to the next step.

(b-4) Case (iv): $p_{iy} \leq 0 \wedge \dot{p}_{ix} < 0$ in the previous step: The elastic body is assumed to slip backward in the $-X$ direction, and the simulation goes to the next step.

Tip position determined by potential energy. In the case where slip is detected in the current step, the tip position of the elastic body is derived. According to the law of energy conservation, the work-energy theorem is thus satisfied. That is, the work done by the robot body motion on the elastic bodies is equal to an increase in kinetic and potential energy of elastic bodies, where the kinetic energy can be ignored because it is negligibly small compared to the potential. Based on the principle of minimum potential energy, the elastic body deforms so that its potential energy is minimized. Here, a non-conservative friction force acting on the tip of elastic body is also involved. Thus, the joint angles of the elastic body can be derived as the solution of the following equation:

$$\frac{\partial}{\partial p_{ix}} \left(U(p_{ix}) + \mu_d \int_{p_{ix0}}^{p_{ix}} N_i(p_{ix}) dp_{ix} \right) = 0. \quad (17)$$

where $U(p_{ix})$ is the potential energy at p_{ix} and p_{ix0} is the reference position.

(c-1) Reference potential energy: As the reference potential energy, the tip position of elastic body in the current step is used. The X-axis component of the tip position is re-defined as $p_{ix} = p_{ix0}$. $U(p_{ix})$ is written as follows:

$$U(p_{ix}) = \frac{1}{2} k_1 \left(\Delta\phi_{1i}(p_{ix})\right)^2 + \frac{1}{2} k_2 \left(\Delta\phi_{2i}(p_{ix})\right)^2, \quad (18)$$

where $\Delta\phi_{1i}(p_{ix})$ and $\Delta\phi_{2i}(p_{ix})$ are the angle variations of the first and second joints, respectively, and they can be represented as functions of p_{ix}. The reference potential energy in the current step is also given as $U(p_{ix0})$.

(c-2) Comparison between $U(p_{ix0})$ and $U(p_{ix})$ with movement of Δp_{ix}: The tip of the elastic position moves a microdistance, Δp_{ix}, from p_{ix0}. The tip position, p_{ix}, is given as $p_{ix} = p_{ix0} \pm \Delta p_{ix}$ in response to the slip direction of the elastic body. In order for the tip position to reach p_{ix}, the sum of $U(p_{ix})$ at p_{ix} and dissipation energy during the movement of Δp_{ix} is needed to be smaller than $U(p_{ix0})$. Thus, the following relation must be satisfied:

$$U(p_{ix0}) > U(p_{ix}) + \mu_d \int_{p_{ix0}}^{p_{ix}} N_i(p_{ix}) dp_{ix}. \quad (19)$$

(c-3) The tip position in the current step: Because the elastic body intends to deform in order to store a lower potential energy, the tip's slippage is changed by adding or subtracting Δp_{ix} and by satisfying Eq. (19). Assuming that there is no limit to migration distance of the elastic body during a calculation

https://doi.org/10.1017/S0263574721000539 Published online by Cambridge University Press

Table 1. *Robot model parameters used in the numerical simulation.*

Symbol (unit)	Value	Symbol (unit)	Value
M (kg)	4.32	μ_s (-)	0.54
I (kgm^2)	0.0154	μ_d (-)	0.19
m_e (kg)	0.634	k_1 (Nm/rad)	7.20×10^{-3}
J_M (kgm^2)	2.75×10^{-4}	d_1 (Nms/rad)	7.20×10^{-7}
r_e (m)	2.16×10^{-3}	k_2 (Nm/rad)	1.20×10^{-3}
K_T (Nm/A)	0.0195	d_2 (Nms/rad)	1.20×10^{-7}
R_M (Ω)	0.165	ϕ_0 (rad)	$7\pi/18$ (= 70.0°)
h_0 (m)	0.02		

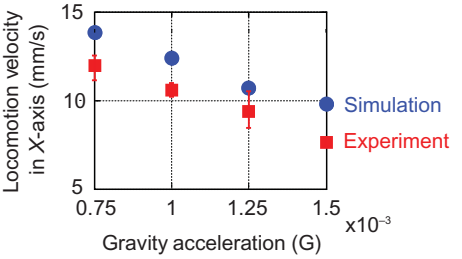

Figure 8. *Comparison result of the robot velocity in the X-axis with $F_M = 0.219$ (N) under several microgravity conditions.*

step, the tip position of the elastic body is changed with slip until the potential energy becomes a local minimal value. This calculated tip position is a final reaching point, and the elastic body is deemed to have velocity.

3.3. Comparison

The dynamics model of vibration propulsion motion is quantitatively evaluated by comparing its numerical simulation with the experimental results. Table 1 shows the model parameters in simulation, where the frictional coefficients were experimentally identified by the slip-slope method based on a dynamic motion analysis.

Regarding a macroscale evaluation, the robot locomotion velocity is discussed. Figure 8 shows the comparison result of the locomotion velocity in the X-axis direction , where the centrifugal force condition is $F_M = 0.219$ (N). The result confirms that the simulation-based relationship between the microgravity and locomotion velocity agrees with the experimental relationship. Quantitatively, the simulation results are close to the experimental values.

Further to the comparison of the macroscale robot motion, microscale behaviors of the elastic body are elaborated. As an analysis on the microscale behavior in the crawling motion, this paper takes up the case of $g = 1.25 \times 10^{-3}$ (G), because the crawling motion was dominantly observed under this gravity condition. Figure 9 shows the comparative time histories of the tip and root positions and angle change of elastic body. From Fig. 9(a), the elastic body performs the stick-slip motion in the simulation and the experiment. Likewise, because the motion profiles of the root show good agreement, the model can adequately simulate the elastic body motion. Considering the resulting time histories of the deformation angle, $\Delta\phi$, shown in Fig. 9(c), the simulation can also represent the experimental behaviors.

https://doi.org/10.1017/S0263574721000539 Published online by Cambridge University Press

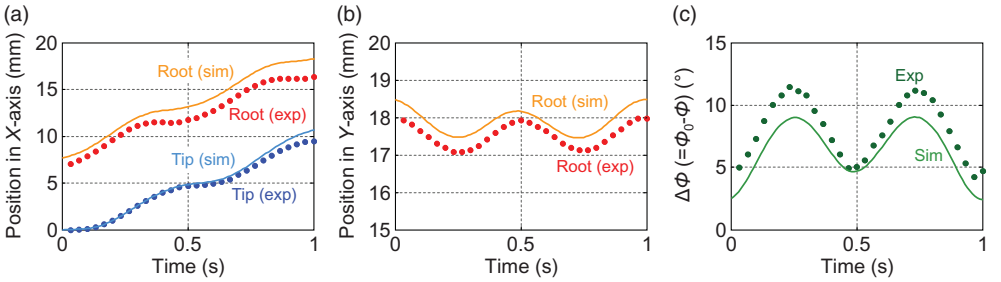

Figure 9. *Comparison results of time histories of the front elastic body in vibration propulsion mode under* $g = 1.25 \times 10^{-3}$ *(G): (a) position in the X-axis, (b) position in the Y-axis, and (c) deformation angle.*

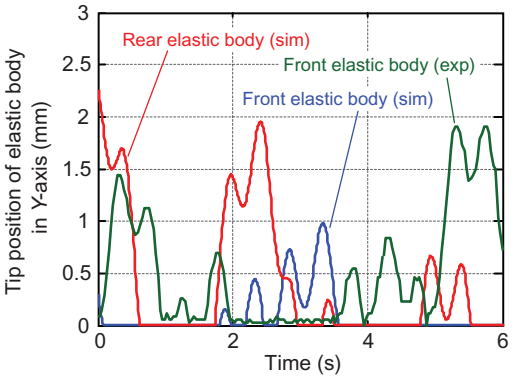

Figure 10. *Comparative time histories of tip position of the elastic body in the Y-axis under* $g = 7.5 \times 10^{-4}$ *(G).*

The microscale behaviors of the elastic body in the micro-hopping motion are now analyzed. The tip position of the elastic body in the Y-axis direction is focused, where the gravity of 7.5×10^{-4} G is discussed. Figure 10 shows the comparative time histories of the tip position. From this result, microscale hopping states are confirmed via both simulation and experiment. The height of the micro-hop in the simulation is inconsistent with the experiment in an exact sense, but it reflects a similar scale and a maximum micro-hop height of approximately 2 mm in both cases. Thus, the developed model can also simulate a micro-hopping motion on a scale similar to the experiment.

Consequently, the comparison results confirm that the dynamics model developed in this paper is validated for the vibration propulsion in microgravity.

4. Rotational hopping

4.1. Motion characteristics

Regarding mobility characteristics of rotational hopping mode, hop velocity and hop angle are analyzed. The hop velocity is defined as hopping velocity of the robot CoM when it loses contact with the ground. The hop velocity in the X- and Y-axes is v_{hx} and v_{hy}, respectively. The hop angle, θ_h, is also defined as $\theta_h = \tan^{-1}(v_{hy}/v_{hx})$. Essentially, the hopping trajectory is dependent on these two parameters, owing to no disturbance. The hop parameters are also affected by microgravity conditions in a precise sense, because of the change of the CoM height above ground based on a balance between the gravitational force and the deformation of the elastic body. However, the height change is negligibly small in microgravity

https://doi.org/10.1017/S0263574721000539 Published online by Cambridge University Press

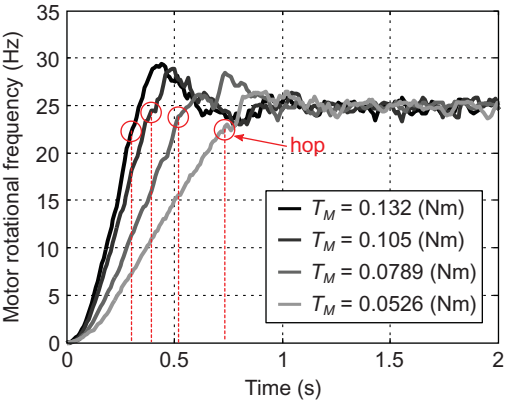

Figure 11. *Time histories of motor rotational frequency for different reaction torque conditions.*

conditions, and the hopping characteristics can be evaluated without gravity effects. Therefore, in this paper, we focus on a typical gravity condition.

4.2. Experimental analysis

4.2.1. Conditions

In the following experiments, the eccentric distance was set to $r_e = 1.0 \times 10^{-3}$ (m). The moment of inertia of the rotating part involving the eccentric weight was 2.51×10^{-4} kgm^2. Furthermore, the frame rate of the recording camera was set to 120 fps for visual observation of the impulsive contact phenomena.

The angular velocity of the motor was controlled based on a proportional-integral-derivative (PID) controller with a control cycle of 100 Hz. Hence, the motor reaction torque was also controlled by the velocity control, so that T_{Md} was constant. Considering specifications of the embedded motor, ω_{Md} was set to 25 Hz. The experimental conditions are summarized below.

- g: 1.25×10^{-3} G
- F_{Md}: 14.31 N
- T_{Md}: 0.0526, 0.0789, 0.105, 0.132 Nm

For each condition, the experiments were conducted five times and the average value was evaluated.

4.2.2. Results and discussion

Figure 11 plots the time histories of the motor rotational frequency for exerting different T_{Md}. In this graph, the point of the starting hop is also depicted. This confirms that an approximately constant motor torque was applied to the testbed until hopping in each condition.

Figure 12 shows a result example of the experimental motion snapshots of rotational hopping under $T_{Md} = 0.132$ (Nm). The motion overview shown in Fig. 12(a) confirms that the testbed can demonstrate rotational hopping motion by controlling the motor rotation. Figure 12(b) shows the close-up view of the square edge at the collision of the ground surface. After the testbed is a static state and starts the motor rotation at $t = 0$ (s), the whole testbed rotates in response to the motor acceleration as the tip of elastic body slips backward. Then, the square edge collides against the ground surface at $t = 0.28$ (s). Owing to the rigid body collision, the edge immediately hops without slip on the surface. Thus, the testbed attitude during the collision can be deemed constant. This confirms the feasibility of the rotational hopping in microgravity by utilizing the reaction torque.

Figure 13 depicts the hop velocity and hop angle results with an error bar against the reaction torque. From Fig. 13(a), the resulting hop velocity is linearly correlated with the reaction torque. Furthermore, Fig. 13(b) shows that the hop angle is approximately constant of 77.3°.

https://doi.org/10.1017/S0263574721000539 Published online by Cambridge University Press

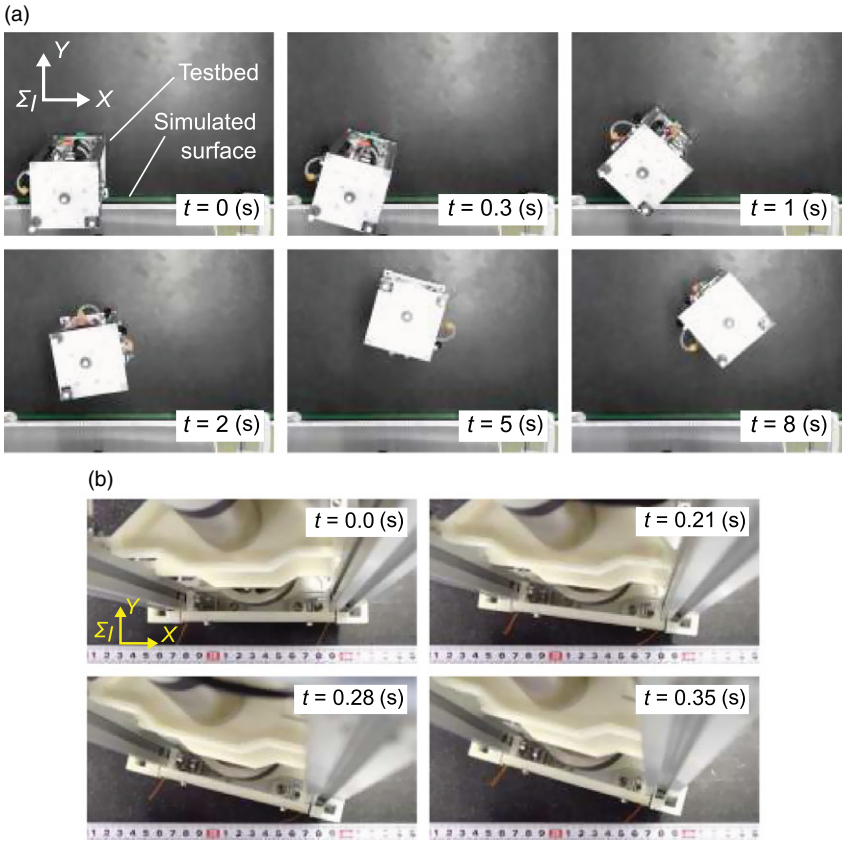

Figure 12. *Experimental motion snapshots of rotational hopping under* $g = 1.25 \times 10^{-3}$ *(G) and* $T_{Md} = 0.132$ *(Nm): (a) motion overview; (b) close-up view at collision.*

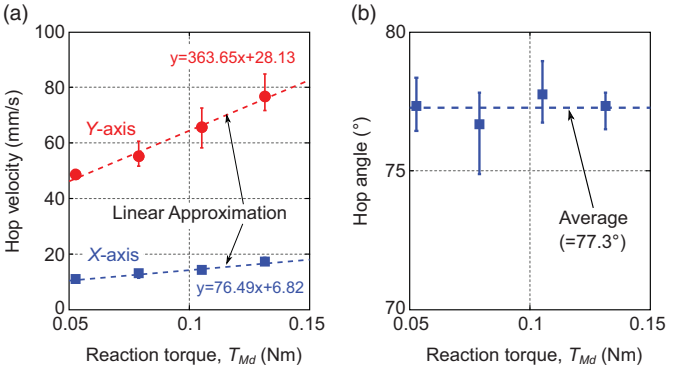

Figure 13. *Experimental results of hopping characteristics under* $g = 1.25 \times 10^{-3}$ *(G) and several reaction torque conditions: (a) hop velocity; (b) hop angle.*

The effects of reaction torque on the hop velocity are now discussed. In the rotational hopping mode, the testbed hops via impulsive rigid collision with the ground surface. Thus, the hop velocity increases with increasing collision impulse. The impulsive force depends on the angular momentum of the testbed just before colliding. Thus, the hop velocity is ultimately proportional to the reaction torque, because the angular velocity of the testbed is given by an integral of the motor acceleration (i.e., the reaction torque). That is, the hop velocity can be actively controlled by changing the reaction torque.

https://doi.org/10.1017/S0263574721000539 Published online by Cambridge University Press

Furthermore, the effects of reaction torque on the hop angle are discussed. Whereas the hop velocity depends on the amplitude of the impulsive force, the hop angle is determined by the direction of the force. Here, a contact angle is defined as the testbed attitude during collision. Geometrically, it is defined as an angle between the ground surface and the line connecting the testbed CoM and the colliding edge. For a rigid collision, the contact angle change can be deeded as constant. In the experiments, the resulting contact angle was within $55° \sim 56°$ regardless of the reaction torque. Therefore, the testbed performed the constant hop angle because the direction of the force was nearly unchanged.

4.3. Modeling

This section elaborates the modeling of rotational hopping to clarify the hopping mechanism by comparing the experimental results.

4.3.1. Equation of motion

Rotational hopping can be achieved, wherein the robot square edge collides with the ground surface. Given that the XY position of this edge is defined as (x_e, y_e) in Σ_I and the reaction force $\boldsymbol{F_g}(F_{gx}, F_{gy})$ acting on the robot CoM, the following equations of motion of the robot CoM are introduced:

$$M\ddot{x} = \sum_{i=1}^{N} F_{fi} + F_{Mx} + F_{gx}, \tag{20}$$

$$M\ddot{y} = \sum_{i=1}^{N} N_i + F_{My} - Mg + F_{gy}, \tag{21}$$

$$\begin{aligned} I\ddot{\theta} = &\sum_{i=1}^{N} \left\{ N_i(p_{ix} - x) - F_{fi}(p_{iy} - y) \right\} + \boldsymbol{v_M} \times \boldsymbol{F_M} \\ &- T_M - F_{gx}(y_e - y) + F_{gy}(x_e - x), \end{aligned} \tag{22}$$

where these equations are applied during contact (i.e., $y_e < 0$).

4.3.2. Contact force

Figure 14 illustrates the contact dynamics model during rigid collision. Assuming a virtual spring-dashpot system in the normal Y-axis direction, the normal contact force, F_{gy}, to the ground can be given as follows:

$$F_{gy} = -k_y y_e - d_y \dot{y}_e, \tag{23}$$

where k_y and d_y are the stiffness and the damping coefficient of the ground in the normal direction, respectively.

Likewise, a linear spring-dashpot-slider system is introduced to simulate the contact force in the tangential X-axis direction as shown in Fig. 14. The tangential contact force, F_{gx}, can be represented as follows:

$$F_{gx} = \begin{cases} -k_x \Delta x_e - d_x \dot{x}_e & \text{for } \frac{|k_x \Delta x_e + d_x \dot{x}_e|}{\mu_{es} F_{gy}} < 1, & \text{(24a)} \\ \mu_{ed} F_{gy} & \text{for } \frac{|k_x \Delta x_e + d_x \dot{x}_e|}{\mu_{es} F_{gy}} \geq 1 \wedge \dot{x}_e \leq 0, & \text{(24b)} \\ -\mu_{ed} F_{gy} & \text{for } \frac{|k_x \Delta x_e + d_x \dot{x}_e|}{\mu_{es} F_{gy}} \geq 1 \wedge \dot{x}_e > 0, & \text{(24c)} \end{cases}$$

where k_x is the tangential stiffness of the ground, d_x is the tangential damping coefficient of the ground, μ_{es} is the static friction coefficient, μ_{ed} is the kinetic friction coefficient, and $\Delta x_e = x_e - x_c$. Here, when

https://doi.org/10.1017/S0263574721000539 Published online by Cambridge University Press

Table 2. *Simulation parameters used in contact dynamics model for rotational hopping.*

Symbol (unit)	Value	Symbol (unit)	Value
k_y (N/m)	10,000	k_x (N/m)	5000
d_y (Ns/m)	150	d_x (Ns/m)	0.5
μ_{es} (-)	0.7	μ_{ed} (-)	0.3

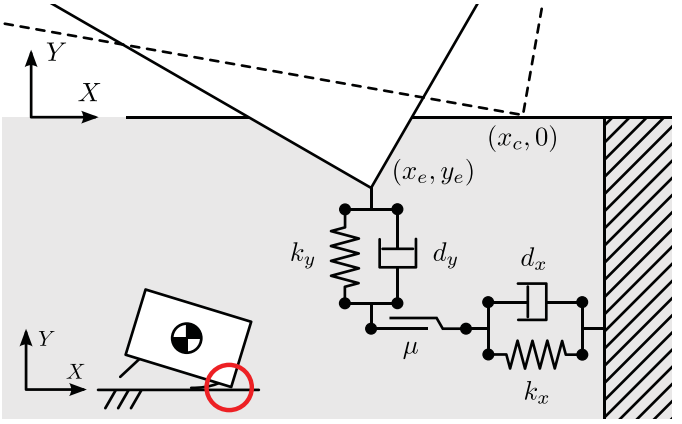

Figure 14. *Contact dynamics model for robot in rotational hopping mode.*

$F_{gy} < 0$, F_{gy} and F_{gx} are given as zero. In the following simulation, we also use the elastic body model described in the previous section.

4.3.3. Determination of simulation parameters

In the following simulation, the parameters shown in Table 1 are commonly used. This section provides a method for determining the ground parameters: stiffness, damping coefficient, and frictional coefficients. These ground parameters used in the simulation are shown in Table 2.

Normal ground parameter. The stiffness, k_y, in the normal direction, was determined in order for the ground to be rigid enough for a time-step for calculation. Based on the balance between an energy loss of the dashpot and an energy loss expressed by a coefficient of restitution, the damping coefficient, d_y, can be given as follows:

$$d_y = \frac{|\ln R_{ey}|\, d_{0y}}{\sqrt{\pi^2 + (\ln R_{ey})^2}}, \tag{25}$$

where R_{ey} (≥ 0) is the coefficient of restitution in the normal direction to the ground and d_{0y} ($= 2\sqrt{Mk_y}$) is the damping constant. To determine R_{ey}, free-fall and bounding motions of the air-floating testbed in planar microgravity were experimentally analyzed based on camera images. The frame rate of the camera was set to 960 fps. From experimental analyses, $R_{ey} = 0.296$ was obtained. Substituting it into Eq. (25), d_y is calculated for simulation.

Tangential ground parameter. In this paper, a typical case of rigid body collision problem of $k_x/k_y = 0.5$ is assumed. d_y was determined such that the hop velocity in the simulation was consistent with its experimental value.

Frictional coefficient. The frictional coefficients between the square edge and the ground surface were experimentally measured by the slip-slope method of a dynamic motion analysis like the vibration propulsion experiments.

https://doi.org/10.1017/S0263574721000539 Published online by Cambridge University Press

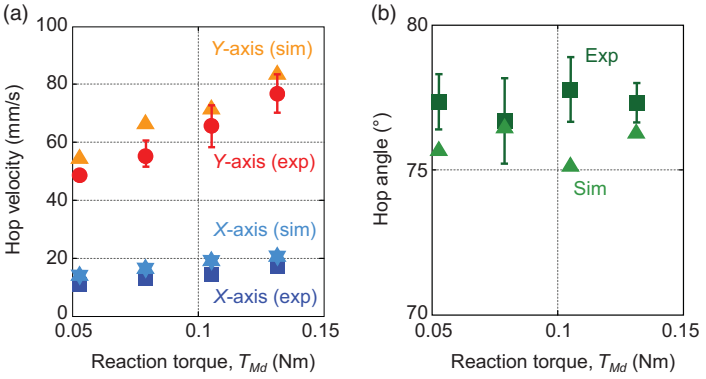

Figure 15. *Comparison results of hopping characteristics under* $g = 1.25 \times 10^{-3}$ *several torque conditions: (a) hop velocity; (b) hop angle.*

4.4. Comparison

The dynamics model of rotational hopping motion was quantitatively evaluated by comparing its numerical simulation with experimental results.

First, the simulation results verified that the developed model can simulate a rotational hopping motion similar to the experimental motion. Figure 15 depicts the comparison of the hopping characteristics by the simulation and experiment. The simulation results in Fig. 15(a) confirm that the hop velocity calculated by the developed model is linearly correlated with the reaction torque, like the experimental plots. Compared to the experimental results, the relative error of simulation was quantitatively an average of 16%. The hop angle results are shown in Fig. 15(b). Regarding the experiment, the hop angle remains about the same with each reaction torque. The relative error of simulation and experiment was 3.1% at maximum. Thus, the developed model is validated for the rotational hopping motion in microgravity.

5. Synthetic analysis

Based on the above results, we discuss a synthetic correlation between the inertial forces (i.e., centrifugal force and reaction torque) and the resulting bimodal mobility performance involving the locomotion mode in microgravity. In the initial step, the bimodal mobility is experimentally examined by changing inertial forces. Then, the synthetic bimodal mobility is analyzed in more detail based on the numerical simulation, and the experimental and simulation results are compared. The inertial forces have implications for the locomotion velocity and mode. Thus, the synthetic correlation is analyzed with the resulting velocity.

5.1. Experimental condition

The experiments were conducted using the common experimental apparatus shown in the previous sections, where the eccentric distance condition was set to $r_e = 1.0 \times 10^{-3}$ (m). Moreover, the motor rotation was also controlled based on F_{Md} and T_{Md}. The experimental conditions are summarized as follows:

- g: 1.25×10^{-3} G
- F_{Md}: 0.37, 1.47, 3.30, 5.86, 9.16 N
- T_{Md}: 0.00158, 0.00316, 0.00632, 0.0126, 0.0253 Nm.

For each condition, the experiments were conducted three times, and the average value was evaluated.

https://doi.org/10.1017/S0263574721000539 Published online by Cambridge University Press

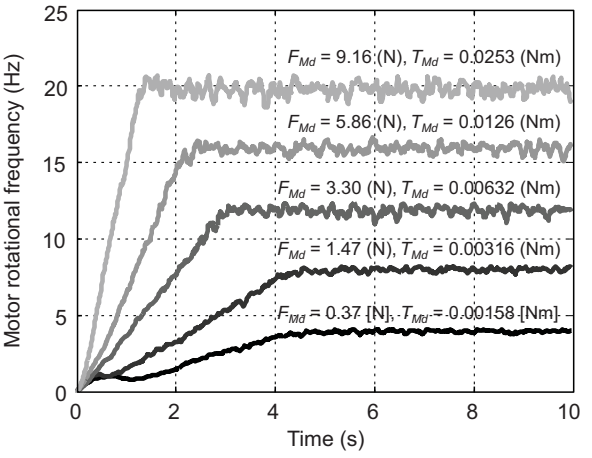

Figure 16. *Time-history examples of motor rotational frequency for changing inertial force conditions.*

Figure 16 plots example results of the time history of the motor rotational frequency in the experiment. Throughout, the motor rotation was adequately controlled to produce each desired inertial force.

5.2. Simulation condition

More precise and in-depth analyses of the synthetic bimodal mobility are now discussed by simulation. Moreover, the simulation analysis helps clarify the transition boundary of the locomotion mode. Furthermore, it yields better understanding of the synthetic correlation of the inertial forces and the resultant locomotion velocity. The common model parameters were set as shown in the previous sections. The simulation conditions are summarized as shown below.

- g: 1.25×10^{-3} G
- F_{Md}: 0, 0.5, 1, $\cdots$, 9, 9.5, 10 N
- T_{Md}: 0, 1.5, 3, $\cdots$, 27, 28.5, 30 mNm

5.3. Results and discussion

Figure 17 shows the experimental and simulation results of the synthetic correlation map of the locomotion mode and the robot CoM velocity in the X-axis direction under $g = 1.25 \times 10^{-3}$ (G). Here, the locomotion velocity was defined as a steady-state value of the robot moving at a steady velocity. In the rotation hopping mode, whereas the robot has the hop velocity in the Y-axis direction, the synthetic analysis focuses on the horizontal velocity parallel to the ground surface to investigate fundamental surface mobility.

5.3.1. Experimental analysis

The experimental result is shown in Fig. 17(a). As seen in the distribution of the resulting locomotion mode, a vibration propulsion mode was generated in the range of relatively smaller inertial forces. In the generation area of the vibration propulsion mode, the crawling motion was shifted to the micro-hopping motion while increasing the centrifugal force. The micro-hopping motion was observed under $F_{Md} = 5.86$, 9.16 (N), because a larger centrifugal force brings a larger attitude change. This result also exhibits the feasibility of switching between the crawling and micro-hopping motion of the motor control.

https://doi.org/10.1017/S0263574721000539 Published online by Cambridge University Press

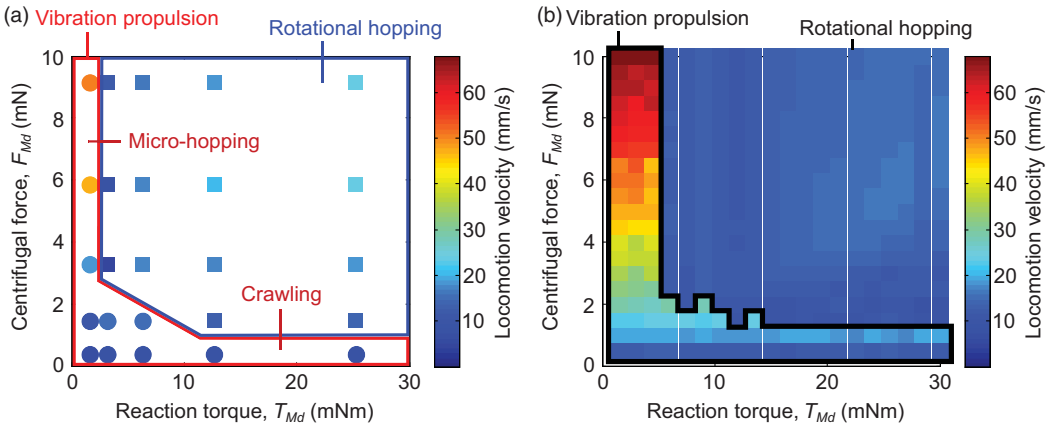

Figure 17. *Synthetic correlation map of locomotion mode and velocity against inertial forces under* $g = 1.25 \times 10^{-3}$ *(G): (a) experiment; (b) simulation.*

The locomotion velocity in each mode is discussed. The vibration propulsion mode assumes a wide range of values from the minimum to maximum locomotion velocities on the correlation map. In this mode, the velocity is evaluated under constant motor rotation. That is, the reaction torque is not affected. From the results, the robot can easily control the locomotion velocity in the vibration propulsion mode via the centrifugal force. Conversely, the locomotion velocity (i.e., the hop velocity in the X-axis) via the rotational hopping is affected by both the centrifugal force and reaction torque, because a larger centrifugal force (i.e., a larger motor rotational velocity) provides a larger angular momentum of the robot in the end, even when the reaction torque is constant. Thus, the locomotion velocity of the rotational hopping mode increases with the increase of inertial forces. However, in some cases, the locomotion velocity makes no difference under different centrifugal forces, because the robot collides with the ground and hops before the motor rotational velocity reaches the desired value, ω_{Md}. Therefore, in the rotational hopping mode, the effects of centrifugal force on locomotion velocity have a certain limit under a constant reaction torque condition.

5.3.2. Simulation analysis and comparison

The simulation result is shown in Fig. 17(b), where the vibration propulsion is generated within the heavy black lines and color-coding corresponds to the amplitude of the locomotion velocity in the X-axis direction. The simulation result provides a clear boundary between the locomotion modes and confirms a continuous velocity change in each. In the case where the reaction torque is not more than 5 mNm, the vibration propulsion is generated regardless of the centrifugal force. Moreover, the locomotion velocity of the vibration propulsion mode is clearly proportional to the centrifugal force. By contrast, in the rotational hopping, the variation of the locomotion velocity is small as with experiments.

Cross-comparison of the experimental and simulation results confirms that the simulation has a good agreement in the qualitative correlation between the inertial forces and the resulting bimodal mobility performance. Additionally, there are minor quantitative differences in both modes, but the differences are within the range of error of the experimental results, shown in the previous sections. Therefore, the developed model is enough to simulate the bimodal mobility in the microgravity. As in other microgravity conditions, this correlation greatly resembles qualitative results, and the simulation provides close agreement with the experimental results.

Throughout the experiment and simulation, the vibration propulsion mode brings a relatively larger locomotion velocity. Furthermore, toward practical applications, the combination of vibration propulsion and rotational hopping is expected to enhance the surface mobility in microgravity. In

https://doi.org/10.1017/S0263574721000539 Published online by Cambridge University Press

particular, control of the inertial forces enables the robot to achieve vibration propulsion by lifting the front elastic body like a motorcycle wheelie motion, which improves obstacle negotiation and avoidance.

6. Conclusion

This paper presented bimodal mobility, vibration propulsion, and rotational hopping, actuated by inertial forces with surface elastic bodies for an exploration robot under microgravity, based on experimental and theoretical analyses. The proposed bimodal mobility was achieved by controlling the centrifugal force and reaction torque of a single eccentric motor, where the rotational hopping is the primary locomotion mode and the vibration propulsion is the secondary one. We experimentally examined the mobility performance of the bimodal mobility system, demonstrating that the bimodal mobility can be selectively generated by the motor control. Moreover, in-depth observation clarified the microscale motion behaviors of the elastic body. Consequently, we established the presence of micro-hopping and crawling motions in the vibration propulsion mode. From the theoretical analysis, the elastic body was modeled for vibration propulsion based on the principle of minimum potential energy. The result showed that the model can simulate microscale motion and gravity effects in experiments. Furthermore, the rotational hopping in the experiments was reasonably simulated based on a rigid collision model. Then, a synthetic correlation between the inertial forces and the resulting bimodal mobility was discussed. The correlation was analyzed through both the experiment and the simulation, and the bimodal mobility mechanism in microgravity was clarified more systematically. As a key result, we verified that the bimodal mobility can be controlled by the inertial forces. In particular, the vibration propulsion was generated by smaller inertial forces and its locomotion velocity was controllable by those forces, whereas the resulting hop velocity and angle of the rotational hopping fall within a relatively small deviation. In summary, the results confirm that the proposed bimodal mobility is feasible in microgravity, and the developed model explains the diverse motion in the experiments.

Future work will extend the bimodal mobility system to more terrain-agnostic mobility systems with spatial motion control. In particular, the hopping mobility is practical to the various terrain and extensible for the spatial motion by the three-axis configuration of the actuators. We have also extended the fundamental concept of the bimodal mobility to a novel torque-based bimodal mobility system with surface elastic bodies [29]. This system can selectively perform hopping and tumbling motion. We will address path planning and motion control with energy efficiency of such a novel mobility system for practical application.

Acknowledgments. This work was partly supported by JSPS KAKENHI Grant Number 24760193.

References

[1] R. Z. Sagdeev and A. V. Zakharov, "Brief history of the Phobos mission," *Nature* **341**, 581–585 (1989).
[2] T. Yoshimitsu, T. Kubota, I. Nakatani, T. Adachi and H. Saito, "Micro-hopping robot for asteroid exploration," *Acta Astronautica* **52**(2–6), 441–446 (2003).
[3] Y. Tsuda, M. Yoshikaw, M. Abe, H. Minamino and S. Nakazawa, "System design of the Hayabusa 2 –asteroid sample return mission to 1999 JU3," *Acta Astronautica* **91**, 356–362 (2013).
[4] T. Yoshimitsu, A. Tomiki and T. Kubota, "Asteroid Surface Exploration Rovers Developed for Hayabusa-2 Mission," *Proceedings of the 66th International Astronautical Congress* (2015).
[5] K. Nagaoka, K. Yoshida, M. Kurisu, K. Osuka, K. Tadakuma, Y. Tsumaki, T. Mineta, S. Kimura, T. Narumi, T. Kubota and T. Yoshimitsu, "Development of MINERVA-II2, a Micro-Robot for Asteroid Surface Exploration with Innovative Mobility," *The 11th Low-Cost Planetary Missions Conference* (2015).
[6] T.-M. Ho, V. Baturkin, C. Grimm, J. T. Grundmann, C. Hobbie, E. Ksenik, C. Lange, K. Sasaki, M. Schlotterer, M. Talapina, N. Termtanasombat, E. Wejmo, L. Witte, M. Wrasmann, G. Wubbels, J. Rosler, C. Ziach, R. Findlay, J. Biele, C. Krause, S. Ulamec, M. Lange, O. Mierheim, R. Lichtenheldt, M. Maier, J. Reill, H.-J. Sedlmayr, P. Bousquet, A. Bellion, O. Bompis, C. Cenac-Morthe, M. Deleuze, S. Fredon, E. Jurado, E. Canalias, R. Jaumann, J.-P. Bibring, K. H. Glassmeier, D. Hercik,

https://doi.org/10.1017/S0263574721000539 Published online by Cambridge University Press

M. Grott, L. Celotti, F. Cordero, J. Hendrikse and T. Okada, "MASCOT–the mobile asteroid surface scout onboard the Hayabusa2 mission," *Space Sci. Rev.* **208**(1–4), 339–374 (2017).
[7] "MINERVA-II1: Images from the surface of Ryugu," (Last accessed on February 21, 2021). [Online]. Available: http://www.hayabusa2.jaxa.jp/en/topics/20180927e_MNRV/
[8] "Three hops in three asteroid days – MASCOT successfully completes the exploration of the surface of asteroid Ryugu," (Last accessed on February 21, 2021). [Online]. Available: https://www.dlr.de/content/en/articles/news/2018/4/20181005_mascot-completes-exploration-ruygu.html
[9] B. H. Wilcox and R. N. Jones, "The MUSES-CN Nanorover Mission and Related Technology," *Proceedings of the IEEE Aerospace Conference* (2000) pp. 287–295.
[10] P. Fiorini and J. Burdick, "The development of hopping capabilities for small robots," *Auto. Rob.* **14**(2), 239–254 (2003).
[11] S. Ulamec, V. Kucherenko, J. Biele, A. Bogatchev, A. Makurin and S. Matrossov, "Hopper concepts for small body landers," *Adv. Space Res.* **47**(3), 428–439 (2011).
[12] B. Hockman, A. Frick, R. G. Reid, I. A. D. Nesnas and M. Pavone, "Design, control and experimentation of internally-actuated rovers for the exploration of low-gravity planetary bodies," *J. Field Rob.* **34**(1), 5–24 (2017).
[13] K. Nagaoka, R. Takano, T. Izumo and K. Yoshida, "Ciliary Micro-Hopping Locomotion of an Asteroid Exploration Robot," *Proceedings of the 11th International Symposium on Artificial Intelligence, Robotics and Automation in Space* (2012).
[14] K. Nagaoka and K. Yoshida, "Modeling and Analysis of Ciliary Micro-Hopping Locomotion Actuated by an Eccentric Motor in a Microgravity," *Proceedings of the IEEE/RSJ International Conference on Intelligent Robots and System* (2013) pp. 763–768.
[15] K. Nagaoka, K. Watanabe, T. Kaneko and K. Yoshida, "Mobility Performances of Ciliary Locomotion for an Asteroid Exploration Robot Under Various Environmental Conditions," *Proceedings of the 13th International Symposium on Artificial Intelligence, Robotics and Automation in Space* (2016).
[16] T. Hatsuzawa, M. Hayase and T. Oguchi, "A linear actuator based on cilia vibration," *Sens. Actuators A Phys.* **105**(2), 183–189 (2003).
[17] P. P. Pott, A. Carrasco and H. F. Schlaak, "Ciliae-based actuator with piezoelectric excitation," *Smart Mater. Struct.* **21**(6), #064010 (2012).
[18] K. Ioi, "A Mobile Micro-Robot Using Centrifugal Forces," *Proceedings of the IEEE/ASME International Conference on Advanced Intelligent Mechatronics* (1999) pp. 736–741.
[19] Z. Ding and B. Ziaie, "Vibration-induced frequency-controllable bidirectional locomotion for assembly and microrobotic applications," *IEEE Trans. Rob.* **25**(5), 1192–1196 (2009).
[20] A. K. Eigoli and G. R. Vossoughi, "Dynamic modeling of stick-slip motion in a legged, piezoelectric driven microrobot," *Int. J. Adv. Rob. Syst.* **7**(3), 201–208 (2010).
[21] F. Becker, S. Boerner and V. Lysenko, "On the Mechanics of Bristle-Bots-Modeling, Simulation and Experiments," *Proceedings of the 41st International Symposium on Robotics* (2014) pp. 1–8. Print ISBN: 978-3-8007-3601-0.
[22] S. Okabe, Y. Yokoyama and G. Boothroyd, "Analysis of vibratory feeding where the track has directional friction characteristics," *Int. J. Adv. Manuf. Tech.* **3**(4), 73–85 (1988).
[23] M. Konyo, K. Isaki, K. Hatazaki, S. Tadokoro and F. Takemura, "Ciliary vibration drive mechanism for active scope cameras," *J. Robot. Mech.* **20**(3), 490–499 (2008).
[24] K. Yoshida, T. Maruki and H. Yano, "A Novel Strategy for Asteroid Exploration with a Surface Robot", *Proceedings of the 34th COSPAR Scientific Assembly* (2002) pp. 281–286.
[25] A. Parness, N. Abcouwer, C. Fuller, N. Wiltsie, J. Nash and B. Kennedy, "LEMUR 3: A Limbed Climbing Robot for Extreme Terrain Mobility in Space," *Proceedings of the IEEE International Conference on Robotics and Automation* (2017) pp. 5467–5473.
[26] K. Nagaoka, H. Minote, K. Maruya, Y. Shirai, K. Yoshida, T. Hakamada, H. Sawada and T. Kubota, "Passive spine gripper for free-climbing robot in extreme terrain," *IEEE Robot. Autom Lett.* **3**(3), 1765–1770 (2018).
[27] A. DeSimone and A. Tatone, "Crawling motility through the analysis of model locomotors: Two case studies," *Eur. Phys. J. E* **35**(9), #85 (2012).
[28] E. Bafekrpour, A. Dyskin, E. Pasternak, A. Molotnikov and Y. Estrin, "Internally architectured materials with directionally asymmetric friction," *Sci. Rep.* **5**, #10732 (2015).
[29] K. Kobashi, A. Bando, K. Nagaoka and K. Yoshida, "Tumbling and Hopping Locomotion Control for a Minor Body Exploration Robot," *Proceedings of the 2020 IEEE/RSJ International Conference on Intelligent Robots and System* (2020) pp. 1871–1878.

Cite this article: K. Nagaoka, T. Kaneko and K. Yoshida (2022). "Bimodal mobility actuated by inertial forces with surface elastic bodies in microgravity", Robotica **40**, 294–315. https://doi.org/10.1017/S0263574721000539